Available online at www.sciencedirect.com

ScienceDirect

journal homepage: www.elsevier.com/locate/he

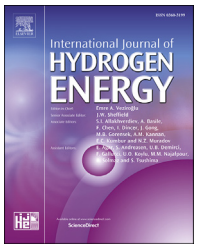

# Hydrogen interaction characteristic of nanoscale oxide films grown on iron–nickel based stainless steel by selective thermal oxidation

*Cheng Zeng* [a], *Yakui Bai* [b], *Yunhan Ling* [a,*], *Zhiyuan Xin* [a], *Hao Liang* [c], *Xiukun Deng* [c]

[a] *Lab of Advanced Materials, School of Materials Sciences and Engineering, Tsinghua University, Beijing 100084, China*

[b] *Institute of Nuclear Fuel and Materials, State Power Investment Corporation Central Research Institute, Beijing 102209, China*

[c] *Institute of Systems Engineering, China Academy of Engineering Physics, Mianyang 621900, China*

ARTICLE INFO

*Article history:*
Received 30 October 2016
Received in revised form
1 February 2017
Accepted 27 February 2017
Available online 19 March 2017

*Keywords:*
Stainless steel
Selective oxidation
Hydrogen annealing
Electrochemistry

ABSTRACT

Hydrogen isotopes, the reaction ingredients in the nuclear fusion plant, can easily permeate through the stainless steel (SS) substrate, leading to the so-called hydrogen degradation. Generally, a widely accepted way to reduce the hydrogen permeation is to prepare a barrier coating on the substrate. Nevertheless, the coated layer has the inherent problem of incompatibility with the heterogeneous base materials. In this work, in-situ selective oxidation was used to explore the optimal oxides with the improved hydrogen resistance. Two types of layers thermally formed at 450 °C and 750 °C, respectively, were selected to investigate their hydrogen interaction characteristics. Comprehensive analyses, including Raman spectra, XPS, EIS and AES, indicate that the oxide formed at 450 °C is a better candidate of hydrogen permeation barriers, probably due to the formation of protective layers of chromia and $FeCr_2O_4$, while the oxides obtained at 750 °C, though exhibiting a much more stable phase, can rarely reduce hydrogen diffusion through the shortcuts of defects. This finding provides a potential new way to prepare a hydrogen permeation barrier.



## Introduction

Iron-nickel based stainless steels (SS) are essential base materials with a host of commercial applications, such as structural materials in nuclear reactors due to their excellent mechanical properties and well-established manufacturing process [1,2]. However, the SS applied in the nuclear plant as the substrate material could barely suppress the hydrogen permeation, which can lead to the leakage of costly ingredients and ensuing radioactive pollution [3]. The most common method to improve the hydrogen diffusion resistivity is applying a tritium permeation barrier on the SS surface, which can mainly be categorized into two groups, i.e. oxide coatings and silicon or titanium based composite

* *Corresponding author*. Fax:+86 106 277 2507.
E-mail address: yhling@mail.tsinghua.edu.cn (Y. Ling).
http://dx.doi.org/10.1016/j.ijhydene.2017.02.206

ceramic coatings [4,5]. For instance, $Cr_2O_3$-$SiO_2$+$CrPO_4$ composite coatings prepared by a slurry and chemical densification method show a permeation reduction factor of about 1000 [6]. In addition, numerous studies suggest that even hundreds of nanometers thick nanoscale films, such as zirconia, alumina and erbia, can act as effective hydrogen permeation barriers [7–10]. Nevertheless, the hetero-interface between external coatings and the base metal is an important issue in extreme conditions during the in-pile operation [11,12].

In order to address the problem of incompatibility between the substrate and coatings, oxides containing similar elements like Fe or Cr and with a transition layer in between were widely studied and showed an enhanced bonding strength [13,14]. Aside from introducing interlayer between the base metal and coatings to increase the adhesion force, in-situ selective oxidation was also proposed as another promising alternative to tackle this issue [15,16]. For example, nanoscale chromia layers were generated on the austenitic stainless steel selectively oxidized under an ultra-high vacuum of ca. $10^{-8}$ torr for up to 20 days, and manifested a treatment reduction factor of as much as 10,000 [17]. This type of in-situ selective oxidation, though somewhat effective, is highly time consuming and demanding for the equipment.

Although massive attempts have been made to suppress the hydrogen treatment through the base metals, to the best of our knowledge, a feasible and cost-effective way is still unavailable. However, noting that the normal operating temperature of first-wall materials implemented in the nuclear fusion reactors is around 350 °C, therefore if oxides formed above this temperature can demonstrate a desirable hydrogen treatment resistance, they can be considered as potential candidates for tritium permeation barriers.

In this paper, the as-received iron-nickel based stainless steels were thermally oxidized for 4 h at temperatures ranging from 250 to 750 °C with one-hundred centigrade intervals, and under a pressure of 1 atm and $10^{-3}$ Pa, respectively. Then oxides formed at 450 °C and 750 °C are selected as subjects for the subsequent hydrogen heat treatment study. Their hydrogen interaction characteristics are compared and comprehensively investigated via surface analysis techniques, including Raman spectra, X-ray Photon-electron Spectroscopy (XPS), Electrochemical Impedance Spectroscopy (EIS). Results indicated that oxide films prepared at 450 °C reflected a higher hydrogen sorption resistance, probably due to the formation of inner dense chromia or $FeCr_2O_4$ spinel barrier, whereas stainless steel oxidized at 750 °C, nevertheless much more stable overall, can barely impede the hydrogen diffusion through the shortcuts of defects.

## Experimental details

The specimens studied in this work are recrystallized stainless steels provided by China Academic of Engineering Physics. The chemical composition (wt.%) is shown in Table 1. The as-received samples were then incised into sheets with dimensions of 20 mm × 10 mm × 1 mm by an electric sparking wire-cut. Samples were mechanically ground with SiC paper of grit sizes ranging from 500 to 5000, and then polished with diamond paste down to 0.5 μm.

**Table 1 – Chemical composition of the as-received stainless steel.**

| Element | Ni | Cr | Ti | Mo | Al | Si | Fe |
|---|---|---|---|---|---|---|---|
| wt.% | 28.49 | 15.37 | 2.26 | 1.38 | 0.67 | 0.15 | Bal. |

Prior to oxidation, the specimens were chemically etched to remove the native oxide films. The specimen is immersed in a dilute aqueous solution composed of 20 vol.% $HNO_3$ and 5 vol.% $H_2SO_4$ for about 10 s and then rinsed with distilled water to remove the residues on the surface. The nanoscale oxide films formed under 1 atm. were obtained using a conventional thermal treatment at different temperatures for 4 h, while oxide layers formed under low pressure were sealed in quartz tubes with air pressure of $10^{-3}$ Pa.

With regards to the hydrogen treatment, the as-prepared samples after oxidation were sealed in quartz tubes with hydrogen pressure of 5000 Pa at room temperature and heated at 400 °C for 2 h, and thus the estimated hydrogen pressure via the ideal gas state equation is about 11,000 Pa.

The microstructure of the as-received alloys was examined by a polarized light optical microscope (OM, 6XB-PC, China) and Electron Back Scattering Diffraction (EBSD) installed on the scanning electron microscopy elaborated in the following. Prior to the observations, the alloys were electrochemically etched using a solution made up of 90 vol.% $C_2H_5OH$ + 10 vol.% $HClO_4$ at a voltage of 0.2 V for 8 min in a water bath with temperature stabilized at 55 °C. Phase identification of the oxide layers was performed with a Raman spectrometer (Lab HR Evolution, HORIBA, France) using argon ion laser excitation at 532.2 nm at room temperature. Surface morphologies of the films were examined by field emission scanning electron microscopy (FE-SEM, JSM-7001F, JEOL, Japan), or atomic force microscopy (AFM, NTEGRA Solaris, NT-MDT, Russia). Depth distribution of different elements was measured by Auger electron spectroscopy (AES, Cypher, OXFORD instruments, UK), equipped with a coaxial electron gun, a differentially pumped Ar ion gun and CMA energy analyzer. X-ray photoelectron spectroscopy (XPS, ESCALAB 250Xi, Thermo Fisher SCIENTIFIC, US) was used with a monochromatic Al X-ray source of 15 kV, 45 W. The pressure during XPS analysis was less than $1 \times 10^{-6}$ Pa and all spectra were referenced to C 1s peak of adventitious hydrocarbon at 284.60 eV [18]. The XPS spectra are curve-fitted with a combination of Gaussian and Lorentzian line shapes, using a Shirley and Linear combined background subtraction.

All the Electrochemical results were recorded in a three-electrode cell with a universal electrochemical interface analyzer (IM6E, ZAHNER, Germany). The samples, which are also the working electrode, were embedded in a two-component epoxy resin with the platinum foil acting as the counter electrode and the saturated calomel electrode (SCE) as the reference electrode. All experiments were performed at ambient temperature in 0.1 M $Na_2SO_4$. The electrochemical impedance spectroscopy (EIS) test was carried out using an excitation voltage of 10 mV (peak-to-peak) and an applied frequency from 1 MHz to 0.01 Hz. The EIS data were analyzed and fitted to appropriate electrical equivalent circuit (EEC) using the software Zsimpwin. For the Mott–Schottky

measurements, the capacitance of the interface was measured at a constant frequency of 1 kHz at a sweep rate of 50 mV/s. It should be noted that all the electrochemical measurements were conducted after holding the open circuit potential for 3 h. The EIS data is tested for three times for verification.

## Results and discussion

### *Morphology and phase analysis*

The optical and EBSD images are shown in Fig. 1. It was clear that the as-received stainless steel exhibited a typical austenitic micro-structure. In addition, the EBSD results confirmed the face-centered cubic (fcc) form of gamma phase with the point group of m $\bar{3}$ m, and the average grain size is estimated to be 24 μm. In addition, one can see from the inverse pole figures that no specific texture is observed.

Raman spectra and the surface morphologies of SS oxidized at temperatures ranging from 250 °C to 750 °C under the air pressure of $10^{-3}$ Pa and 1 atm are shown in Fig. 2. It indicates that at atmospheric pressure and with temperature below 550 °C, the oxides are mainly composed of hematite, and spinel of magnetite and $NiFe_2O_4$, while if the temperature is above 550 °C, for instance 650 °C and 750 °C, the oxides are predominately made up of composite spinel and chromia, which is consistent with previous results [19,20]. However, under the pressure of $10^{-3}$ Pa, the oxidation proceeded much more slowly. Only scattering oxide particles were observed on the surface below 550 °C even though Raman spectra displayed a well-defined peak for the 450 °C sample. In terms of oxides obtained at 650 °C and 750 °C, despite the formation of large patches of oxides, the Raman spectra suggested that no crystalline phase was generated. Given that a satisfactory hydrogen permeation barrier should be of desirable thickness, oxides obtained under the atmospheric pressure were thus chosen as the subjects in the following discussion. For simplicity, specimens with and without hydrogen heat treatment are denoted as YH and NH, respectively.

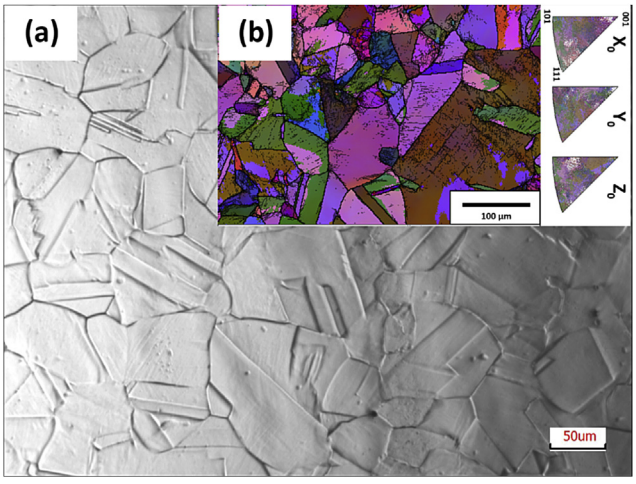


**Fig. 1 – Optical (a) and EBSD (b) images of the as-received stainless steel.**

Fig. 3 shows the Raman spectra and AFM images of the oxides formed at 450 °C and 750 °C with and without hydrogen annealing. It is well documented in literature that the Raman peaks at 223, 243, 290, 410, 503 and 612 $cm^{-1}$ can be well ascribed to the phase of hematite, while the peak at ca. 662 $cm^{-1}$ belongs to magnetite and $NiFe_2O_4$ spinel [20,21]. Therefore, the 450-NH mainly constituted of hematite and spinel like phases, whereas Raman spectrum of 450-YH displayed the phase of $NiFe_2O_4$ and chromia. Nevertheless, the surface morphology remained unaltered. As for oxides formed 750 °C, it appeared that the phase kept unchanged, i.e. both 750-NH and 750-YH are composed of chromia, and composite spinel, which may contain Ti, Cr, Ni and Fe elements. In terms of the surface morphologies presented by AFM, it is estimated that the surface roughness of oxides obtained at 450 °C after hydrogen heat annealing shows a decrease, whereas that obtained at 750 °C was increased after hydrogen treatment. The average surface roughness of 450-NH and 450-YH is around 20 and 14.2 nm, while the surface roughness of 750-NH and 750-YH are 44.6 and 47.7 nm, respectively.

### *Electrochemical measurement*

#### *EIS measurements*

Fig. 4 presents the observed and fitted EIS bode plots of the oxide layers with and without hydrogen heat treatment. It is clear that for oxides formed at 450 and 750 °C, the magnitude of impedance shows a decline by ca. 60% with hydrogen annealing. In terms of the phase angle change, it can be seen from Fig. 4 that at frequency larger than ca. 10 Hz, the phase angle increases with the decreasing frequency, while it exhibits a decrease when the frequency is lower than ca. 10 Hz. Comparing the phase angle change of oxides formed at 450 and 750 °C, one can see that the phase angle of 450-YH at low frequency such as 100 and 10 mHz is higher than that of 750-YH, which suggests that oxides formed at 450 °C can be more protective than that formed on 750 °C.

Judging from the above-mentioned and subsequent results in Subsections Thermodynamic analysis and chemical states and Oxide structure, the corresponding Randles equivalent circuits (EC) were employed to fit the curve and provide some insights into the impedance plots. The applied EC is shown in Fig. 5. The EIS plots for 450-NH could be best fitted by the equivalent circuit consisting of Rs in series with three parallel combinations of resistance and constant phase element, whereas taking into account the reduction of iron oxides after hydrogen heat treatment, the impedance diagram of 450-YH could be resolved to just two resistive layers (Fig. 5(b)). As for 750-NH and 750-YH, the corresponding EIS plots can also be well fitted using the EC shown in Fig. 5(b). The values of each parameter and its corresponding error are summarized in Table 2, namely solution resistance ($R_S$), the resistance and constant-phase element of outer oxide layer ($R_1$ and $Q_1$), inner oxide layer ($R_2$ and $Q_2$), and the intermediate layer (Ri and Qi, if existent), respectively. Since the contribution of intermediate layer to the hydrogen resistance can be neglected, compared to inner relative dense layer, the fitted values of Ri and Qi are not listed. It can be seen from Fig. 4 that all the EIS plots are well fitted using the proposed EC, with the overall squared error less than 0.001. Compared to750-NH, it is clear that value

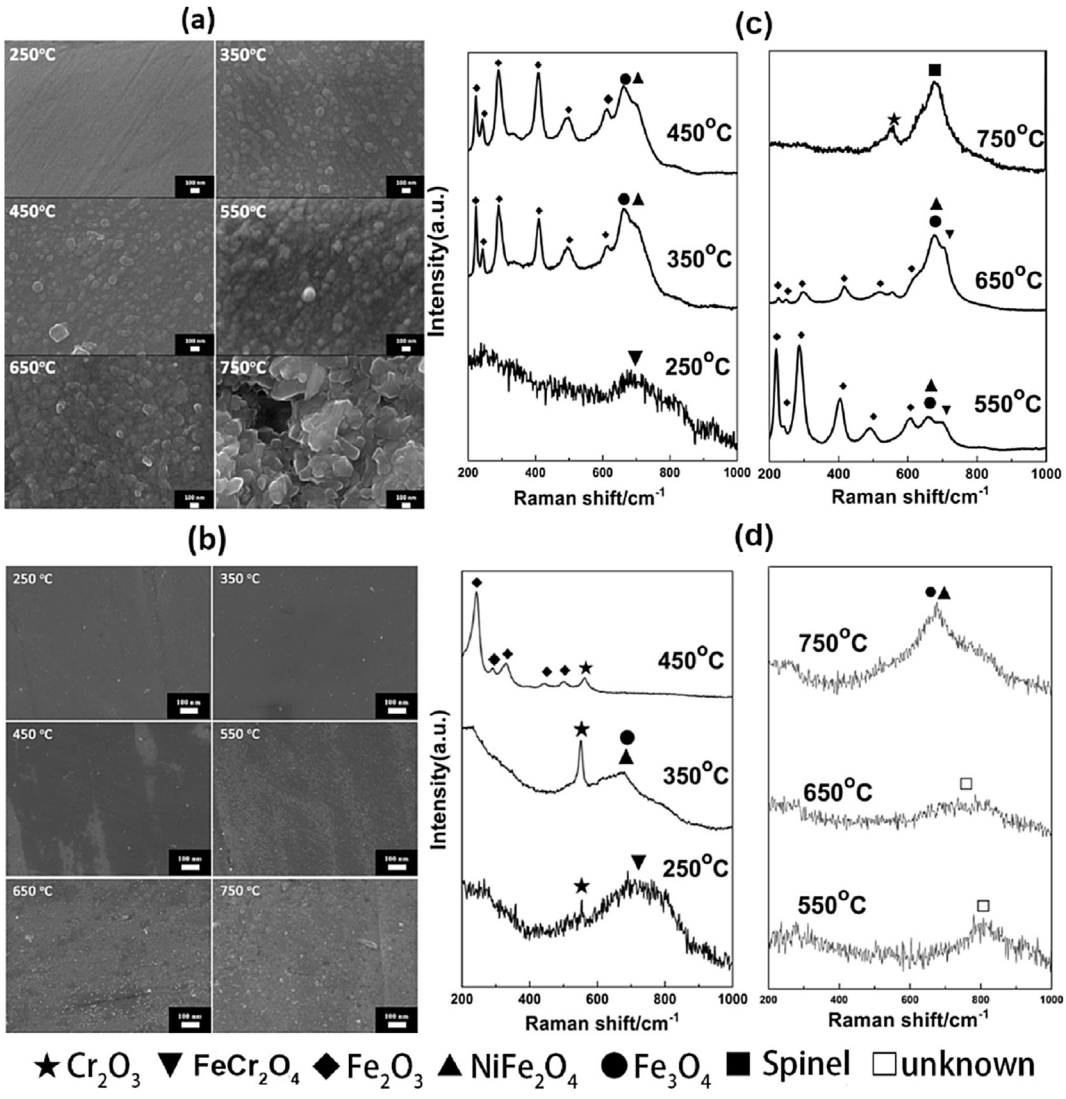


**Fig. 2 – SEM images and Raman spectra of SS oxidized at temperatures ranging from 250 °C to 750 °C under the air pressure of 1 atm and $10^{-3}$ Pa: (a) surface morphologies of oxides grown under air pressure of 1 atm, (b) surface morphologies of oxides grown under air pressure of $10^{-3}$ Pa, (c) Raman spectra of oxides grown under air pressure of 1 atm, and (d) Raman spectra of oxides grown under air pressure of $10^{-3}$ Pa.**

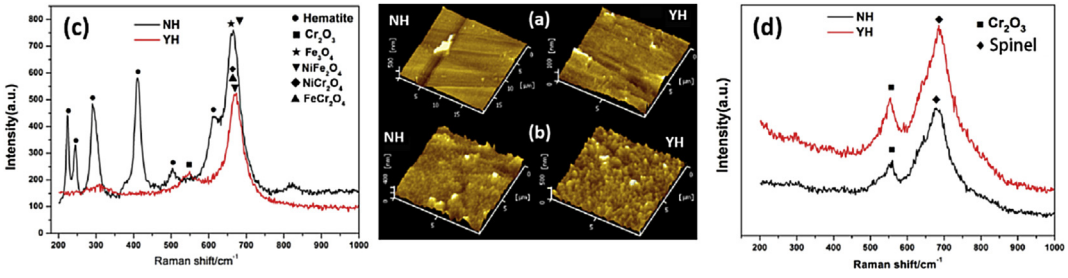


**Fig. 3 – AFM images and Raman spectra for oxides formed at 450 °C and 750 °C with and without hydrogen annealing: (a) AFM images for oxides formed at 450 °C, (b) AFM images for oxides formed at 750 °C, (c) Raman spectra or oxides formed at 450 °C, and (d) Raman spectra or oxides formed at 750 °C.**

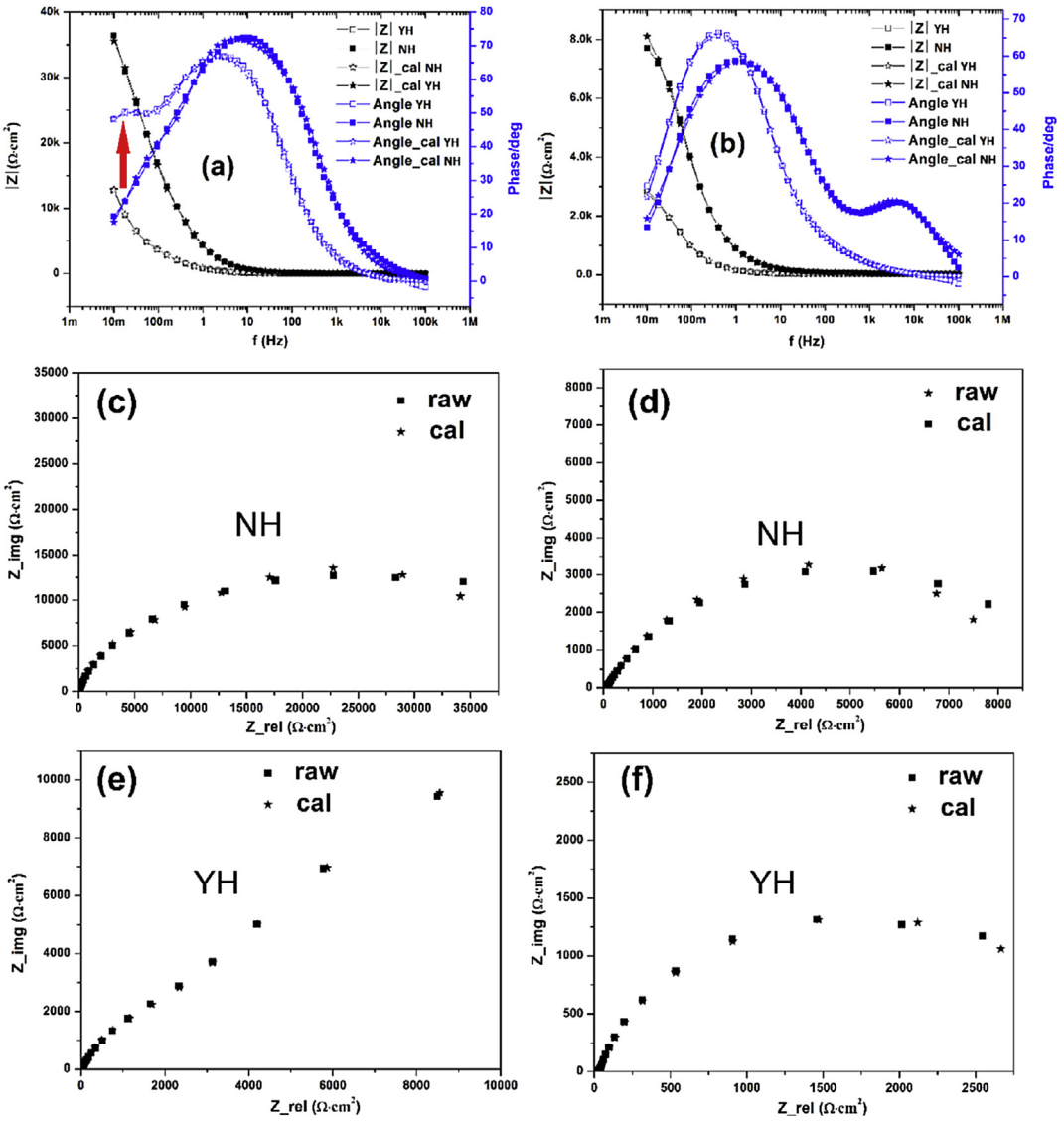


**Fig. 4 – Bode and Nyquist plots of the oxide layers formed at 450 °C and 750 °C with and without hydrogen annealing: (a) Bode plots for oxides formed at 450 °C with and without hydrogen annealing, (b) Bode plots for oxides formed at 750 °C with and without hydrogen annealing, (c) Nyquist plots for oxides formed 450 °C without hydrogen annealing, (d) Nyquist plots for oxides formed 750 °C without hydrogen heat treatment, (e) Nyquist plots for oxides formed 450 °C with hydrogen heat treatment, and (f) Nyquist plots for oxides formed 750 °C with hydrogen heat treatment.**

of R is lower for 750-YH. In contrast to the oxides formed at 750 °C, oxides formed at 450 °C shows a 44% increase of resistance from 32.5 to 46.8 kΩ $cm^2$, which is in good accordance with above-mentioned phase variation in the lower frequency range, and confirms the effectiveness of the phase angle analysis.

*Mott–Schottky analysis*

Mott–Schottky measurements were carried out to investigate the semiconductor properties of the nanoscale oxide films. Generally, according to Mott–Schottky (MS) theory [22], the space charge capacitances of n-type and p-type semiconductors are approximately given by

$$\frac{1}{C_{sc}^2} = \frac{2}{\varepsilon\varepsilon_0 q N_D}\left(V - V_{fb} - \frac{kT}{q}\right) \quad n-type \tag{1}$$

and

$$\frac{1}{C_{sc}^2} = \frac{-2}{\varepsilon\varepsilon_0 q N_A}\left(V - V_{fb} - \frac{kT}{q}\right) \quad p-type \tag{2}$$

Respectively, where $N_D/N_A$ is the donor/acceptor concentration ($cm^{-3}$), $\varepsilon_0$ is the vacuum permittivity (8.85 × $10^{-14}$ F/cm) and $\varepsilon$ is the relative dielectric constant of the corresponding passive film. It is assumed that the dielectric constant of films with hydrogen annealing remains unchanged. k is the Boltzmann constant (1.38 × $10^{-23}$ J/K) and $T$ is the Kelvin

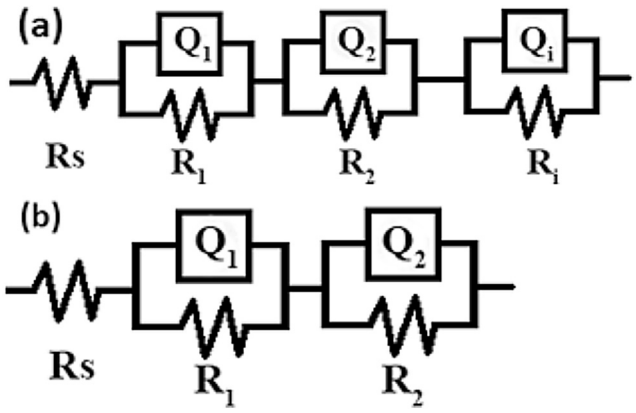


**Fig. 5 – Randles equivalent circuits for the EIS spectra of 450-NH (a), and other oxides (b).**

temperature. V is the applied potential, $V_{fb}$ is the flat band potential, $q$ is the electron charge ($1.6 \times 10^{-19}$ C), and $kT/q$ is about 25 mV at room temperature. According to the values well-documented in the literature, the relative dielectric constants of chromia and iron oxides in this work are assumed to be similar to the values of the stoichiometric corundum-like $Cr_2O_3$ and hematite, i.e. 12 and 14.2, respectively [23,24].

Fig. 6 shows the M–S plots for oxides formed at 450 and 750 °C with and without hydrogen annealing. Taking Fig. 6(a) of NH for example, one can see that it exhibited two linear regions with a negative and positive slope separated by narrow potential plateau. Judging from Eqs. (1) and (2), the region of straight line with a negative slope indicates the presence of a p-type semiconductor property and vice versa. The shape of M–S plots of 450-NH is in consistent with previous studies [25–27].

Theoretically, if the total electron number in the conduction band of oxides is larger than that of holes in the valence band, the oxides could be taken as an n-type semiconductor, such as ZnO, $TiO_2$, and $WO_3$. Conversely, it is a p-type semiconductor such as NiO, $Cr_2O_3$ and $Cu_2O$. Numerous researches suggest that the oxides formed on SS display composite semiconductor properties [25,28]. It is also concluded that the specific semiconductor properties are closed correlated to the predominant defects in the films. Films with a deficiency in metallic ions or excess of cation vacancies can lead to p-type semiconductors while n-type ones evolve in the films deficient in cation ions or doped by interstitial anions.

On the basis of the electronic band theory mentioned above and the observed experimental results, the M–S plots in this study can thus be explained as the following discussion. With regards to the 450-NH, the n-type properties could be attributed to the iron oxide species ($Fe_3O_4$, $Fe_2O_3$ and $NiFe_2O_4$) whereas the p-type component could be assigned to the formation of $Cr_2O_3$, FeO or spinel oxides such as $FeCr_2O_4$ [27]. After hydrogen treatment, the obtained 450-YH merely reflected the feature of n-type semiconductor, which is probably caused by the reduction of iron oxides and the hydrogen-induced oxide vacancies in the inner oxide layers. Nevertheless, in terms of the M–S plot of 750-NH, the oxide layer presents almost an exclusive p-type property, which agrees well with the phase composition of chromia, and chromium-related spinel. Additionally, the oxides were partially reduced to n-type oxides after the hydrogen heat treatment, leading to the formation of n-type and p-type mixed structure. According to the slopes of the fitted linear region, carrier concentrations were calculated and listed in Table 3. The values of $N_A$ and $N_D$ are in the order of magnitude $10^{20}$ $cm^{-3}$ for the as-prepared oxides formed at both 450 °C and 750 °C. The magnitude of the carrier concentration is comparable with the results reported previously [25,29].

As can be seen in Table 3, although the semiconductor type for oxides formed at 450 °C changed from p-type to n-type after hydrogen heat treatment, the total carrier density for certain oxides decreased by 2 orders of magnitude. However, as for oxides formed at 750 °C, despite the growth of total thickness of the layer, the carrier density for p-type layer with hydrogen annealing is two orders of magnitude larger than that without hydrogen annealing.

### *Thermodynamic analysis and chemical states*

To further substantiate the above-mentioned discussion and reveal the exact structure of the oxides with and without hydrogen heat treatment, AES depth profiles related to the atomic concentration of involved elements and XPS depth analysis revealing the electronic states of O1s, Fe2p, Ni2p, Ti2p and Cr2p were implemented. In order to investigate the oxide growth mechanism, the formation energy and reduction energy of some oxides are summarized in Tables 4 and 5, respectively. It is clear that the absolute formation energy follows the descending order of $TiO_2$, $Cr_2O_3$, $Fe_2O_3$, FeO and NiO, while their tendency to be reduced follows an opposite order. However, it should be noted that the oxide growth is a kinetic process and thus closely associated with a variety of factors, including the type and concentration of alloying elements, the physical and chemical adsorption of oxygen, the defect chemistry, strain and diffusion of cations and anions.

AES depth profiles for oxides obtained at 450 and 750 °C with and without hydrogen heat treatment were shown in

**Table 2 – Equivalent circuit parameter values for oxides with and without hydrogen annealing.**

| Samples | $R_s$(Ω)/E[a] | $Q_1$-T (mF)/E[a] | $Q_1$-P/E[a] | $R_1$(Ω)/E[a] | $Q_2$-T (mF)/E[a] | $Q_2$-P/E[a] | $R_2$(Ω)/E[a] |
|---|---|---|---|---|---|---|---|
| 450-NH | 28/0.76 | 0.065/11 | 0.87/3.0 | 9125/25 | 0.14/21 | 0.83/5.3 | 32,500/10 |
| 450-YH | 24/0.36 | 0.51/2.5 | 0.88/1.8 | 1741/8.8 | 0.60/3.2 | 0.75/0.78 | 46,820/8.2 |
| 750-NH | 20/1.6 | 0.034/18 | 0.70/2.7 | 38/3.0 | 0.29/1.1 | 0.74/0.5 | 9577/1.9 |
| 750-YH | 24/0.46 | 2.43/27 | 0.63/6.2 | 9.6/9.4 | 1.4/0.58 | 0.85/0.42 | 3398/1.4 |

[a] E: error (%).

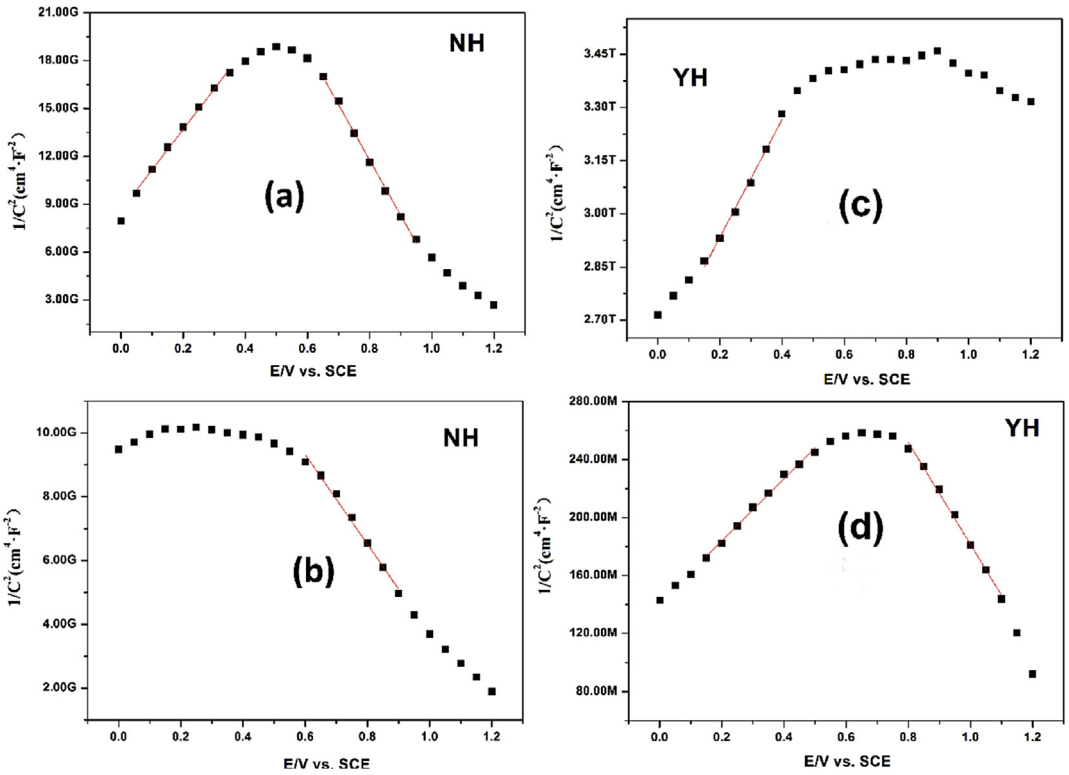


**Fig. 6 – Mott–Schottky (M–S) plots for the oxides formed at 450 °C and 750 °C with and without hydrogen exposure: (a) M–S plots for oxides formed at 450 °C without hydrogen annealing, (b) M–S plots for oxides formed at 750 °C without hydrogen annealing, (c) M–S plots for oxides formed at 450 °C with hydrogen annealing, and (d) M–S plots for oxides formed at 750 °C with hydrogen annealing.**

**Table 3 – The semiconductor types and their calculated carrier concentration for oxides formed at 450 °C and 750 °C with and without hydrogen annealing.**

| Samples | $N_D$ ($10^{20}$ $cm^{-3}$)/E[a] | $N_A$ ($10^{20}$ $cm^{-3}$)/E[a] |
|---|---|---|
| 450-NH | 3.9/2.9 | 3.4/2.1 |
| 450-YH | 0.071/4.1 | – |
| 750-NH | – | 8.4/4.3 |
| 750-YH | 551/3.0 | 335/3.2 |

[a] E: error (%).

**Table 5 – Gibbs free energy of reduction of single oxides at 400 °C with $p_{H_2} = 1.1 \times 10^4 Pa$ and assumed $p_{H_2O} = 1 \times 10^5$ Pa, corresponding to 1 mol $H_2$.**

| | $Cr_2O_3$ | $TiO_2$ | $Fe_2O_3$ | $Fe_3O_4$ | FeO | NiO |
|---|---|---|---|---|---|---|
| $\triangle G_T$ (kJ/mol) | 118 | 141 | 15 | 36 | 19 | −17 |

Fig. 7. The oxides with and without hydrogen heat treatment are denoted with solid and dash lines, respectively. From Fig. 7(a), one can see that for 450-NH, the surface was enriched in Fe with Cr underneath the surface near the oxide/metal interface, which is in good agreement with the observed Raman spectra and previous literature [30,31]. The effective oxide thickness for 450-NH and 450-YH derived from an empirical method is estimated to be 44.5 nm, i.e. we take the distance from the oxygen content of 100% to the oxygen content of 30% as the thickness of the oxides [30]. However, when the temperature is raised to 750 °C, the surface is enriched in Cr elements, then Fe and Ni elements. The thickness of 750-NH is more than four-folds higher than that of 450-NH, and the thickness grows to 367.5 nm for 750-YH. It is inferred that the increase of oxide thickness resulted from the residue absorbed oxygen and ensuing generated water steam in the reductive atmosphere, which is likely due to the less compact structure of 750-NH as indicated by the surface roughness. The oxygen and possible water steam then proceeded to react with the metallic ions during hydrogen heat treatment. Hultquist et al. once reported that the major parameter determining the Cr enrichment is the diffusion of

**Table 4 – Gibbs free energy of formation (kJ/mol) of oxides formed at 450 °C (723 K) and 750 °C (1023 K), corresponding to 1 mol $O_2$.**

| | $Cr_2O_3$ | $TiO_2$ | $Fe_2O_3$ | $Fe_3O_4$ | FeO | NiO | $FeCr_2O_4$ | $NiFe_2O_4$ |
|---|---|---|---|---|---|---|---|---|
| 723 K | −624 | −714 | −417 | −462 | −428 | −356 | −607 | −412 |
| 1023 K | −573 | −760 | −367 | −420 | −392 | −304 | −557 | −360 |

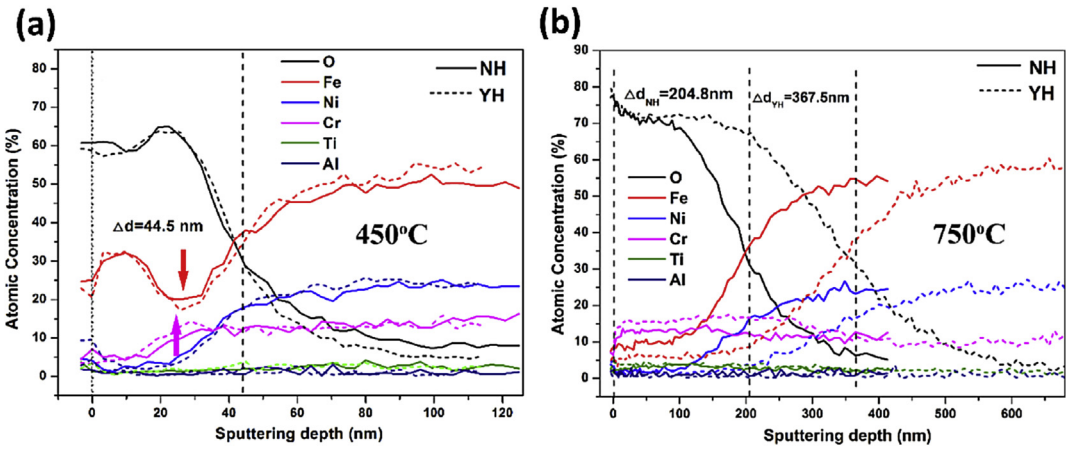


**Fig. 7 – AES depth profiles for oxides formed at 450 °C (a) and 750 °C (b) with and without hydrogen permeation.**

alloying elements from bulk to the gas/oxide interfaces and the partial oxygen pressure at the interface [32]. In our case, comparing the Cr content without and with hydrogen heat treatment, it appears that in the reductive atmosphere Cr tends to diffuse outward preferentially and intensify its segregation in the oxides.

X-ray photoelectron spectroscopy is performed to semi-quantitatively analyze the chemical state of the major elements on the surface. It is well documented that the spin–orbit splitting between the $2p_{3/2}$ and $2p_{1/2}$ peak is of 13.5 eV for Fe, 17.9 eV for Ni, a 9.8 eV for Cr, and 5.7 eV for Ti, respectively [33,34].

The curve deconvolution of the XPS spectra for different photoelectrons was performed and the corresponding percentage of identified components was calculated. From the fitting results of narrow spectra at the surface (Fig. 8), one can see that for 450-NH, the full range survey shows the exclusive presence of Fe2p, and the narrow scan of Fe2p spectrum exhibits three main peaks at 717.83, 711.91 and 709.942 eV, which are probably attributed to the $Fe_3O_4$, $Fe_2O_3$ and $NiFe_2O_4$. The multi-peak fitted spectra of 450-YH are depicted in Fig. 8(b). It shows two peaks at 715.66 and 711.02 eV, which can be attributed to the reduced spinel phase and $O_2$/Fe/Ni species [35]. The result indicates a negative chemical shift compared to that of 450-NH. As for the oxides formed at 750 °C, there are mainly two identified anion species in both spectra at the surface, i.e. the peaks corresponding to $Ti2p_{3/2}$ and $Cr2p_{3/2}$. Also, it is obvious that compared to750-NH, the core levels of both $Ti2p_{3/2}$ and $Cr2p_{3/2}$ spectra increased to a higher binding energy, which suggests that oxidation proceeded, probably due to the absorbed oxygen and resulting water steam in the reductive atmosphere.

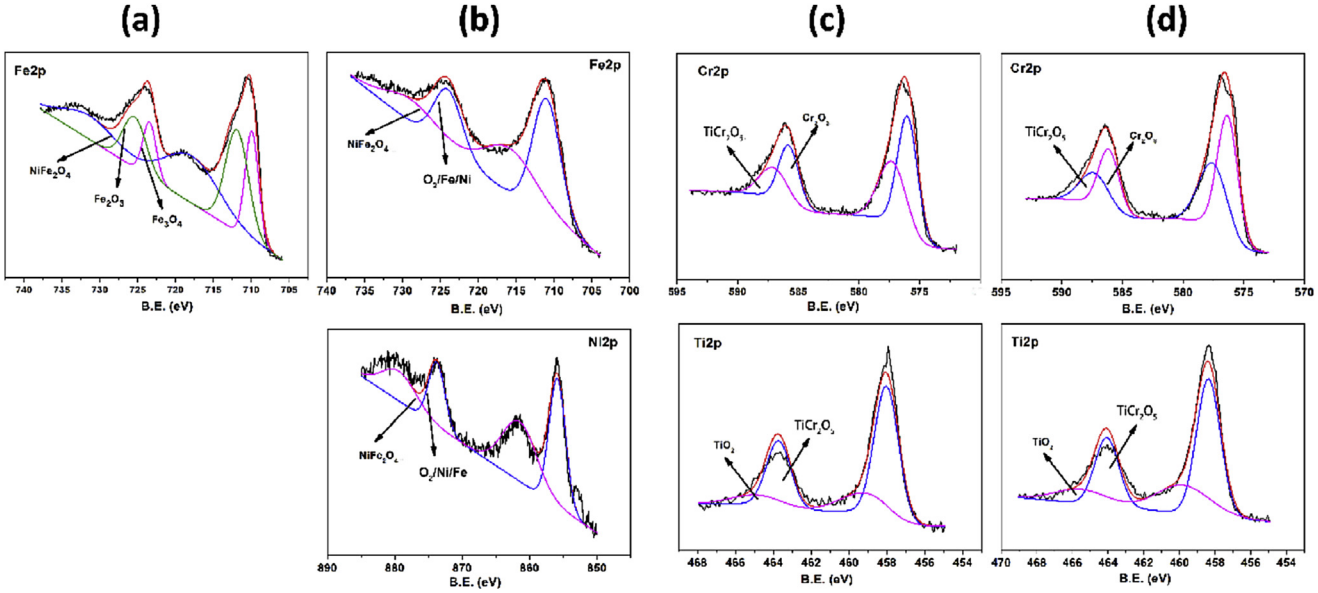


**Fig. 8 – Multi-peak fitted XPS spectra of cations in the oxides formed at 450 °C and 750 °C with and without hydrogen permeation: (a) 450-NH, (b) 450-YH, (c) 750-NH, and (d) 750-YH.**

In addition, the XPS depth analyses (see Figs. S1–S4) indicate that for the 450-NH, nickel oxides can be identified at the surface. But only the metallic nickel species could be identified within the oxides, and so is the 750 °C-NH [35,36]. Also, the depth profile confirmed that both oxides formed at 450 °C and 750 °C are composed of iron oxides, titanium or chromium related oxides, and both are of a transitional oxygen/metal ratio of the chemical composition from the oxide/gas interface to the metal/oxide interface.

In order to assess the chemical state shift of specific photoelectron with and without hydrogen heat treatment, an approximate method was employed to estimate the average binding energy values (denoted as$\overline{BE}$) of relevant elements in the oxides whose XPS plots could be de-convoluted to multi core levels [37]. It is specified as the following equation.

$$\overline{BE} = \sum_{1}^{i}(BE_i \times w_i\%) \quad (3)$$

Where, $BE_i$ is the binding energy values of each identified component and $w_i$% is the corresponding percentage. The calculated $\overline{BE}$ s for oxides formed at 450 °C and 750 °C at different sputtering depth are listed in Tables 6 and 7, respectively. It is evident that iron oxides of 450-NH were reduced after hydrogen annealing.

In addition to XPS profiles of photoelectrons belonging to cations, it should be noted that for the oxides with hydrogen annealing, the O1s depth profiles of 450-YH and 750-YH could be well fitted to two peaks with core-levels centered at ca. 530.3 eV and 531.7 eV, which can be assigned to $O^{2-}$ and possible hydroxide. The hydroxide peak is also shown in other works [38,39], which can somewhat be used to indirectly reflect the existence of hydrogen in the films.

### *Oxide structure*

Based on the comprehensive surface analyses, oxide structures of 450-NH and 750-YH are illustrated. We firstly discussed the possible growth mechanism of each involved isolated mono oxide. According to the Fe-O binary phase diagram, for the pristine iron, the iron oxide is composed of an inner magnetite and outer hematite at 450 °C, while at 750 °C the oxide constitutes a triple layer, i.e. wustite-magnetite-hematite from the inside to the outside oxides. Since the wustite and magnetite are highly deficient in iron cations and thus the self–diffusion coefficient of $Fe^{2+}$ and $Fe^{3+}$ is much larger than that of oxygen, and thus the oxidation behavior of wustite and magnetite shows an outward feature. Although the diffusion coefficient of iron ions are closely related to the defect concentration, the magnitude of self–diffusion coefficient of iron ions in FeO is in the order of $10^{-9}$ ~ $10^{-7}$ $cm^2/s$ at 1000 °C [40]. As for the magnetite $Fe_3O_4$, the diffusion coefficient of iron ions at 1200 °C with oxygen partial pressure of 14 Pa is in the order of $10^{-8}$ $cm^2/s$ [41]. For the corundum-like hematite layer, at the temperature of concern the oxygen migrates faster than iron ions, indicating an inward oxidation mechanism [42–44]. For the oxidation of pure nickel, it is quite similar to that of wustite because of the formation of rock-salt structure NiO, which is a p-type oxide in its electronic nature. For NiO, at 1500 K with an enriched oxygen environment, the (self) diffusion coefficients for nickel and oxygen are in the order of $10^{-9}$ $cm^2/s$, and $10^{-12}$ $cm^2/s$, respectively [45]. As for chromium, the most stable phase is the corundum-like eskolaite, which also shows a p-type character. The self–diffusion coefficient of both oxygen and chromium ions is much smaller than that in wustite and NiO, which means that the oxidation rate is much slower compared to iron and nickel. For instance, at 1300 °C with partial oxygen pressure of $1.01 \times 10^{-5}$~1.01 Pa, the (self) diffusion coefficient of chromium and oxygen in $Cr_2O_3$ is $10^{-19}$ and $10^{-17}$ $cm^2/s$, respectively [46]. Therefore, its oxidation mainly occurs at the inner side of the composite oxides. As for titanium, it generally forms n-type oxides with deficiency in oxygen, thus it follows the process of internal oxidation, which means that oxidation occurs mainly in the inner layer as well. Nevertheless, considering the trace amount of titanium, it is only taken as doping elements for 450-NH.

It should be noted that the aforementioned growth mechanism of each involved single oxide is based on the prerequisite that the oxide layers are compact with no linear or planar defects such as dislocation or grain boundary, and no compound oxides formed. Yet, it is quite common to generate spinel-like phases such as $NiFe_2O_4$ and $NiCr_2O_4$. Moreover, due to the incompatibility between the oxides and the substrate it

**Table 6 – Summary of calculated average binding energy values of core levels of different photoelectrons for oxides formed at 450 °C.**

| Photoelectron type | Thickness (nm) | $\overline{BE}_{NH}$ (eV) | $\overline{BE}_{YH}$ (eV) |
|---|---|---|---|
| 450°C-Fe 2p3/2 | 0 | 713.6 | 712.9 |
| | 10 | 711.5 | 709.1 |
| | 25 | 708.9 | 708.5 |
| | 40 | 708.5 | 708.2 |
| 450°C-Cr 2p3/2 | 10 | 576.5 | 576.2 |
| | 25 | 575.6 | 574.7 |
| | 40 | 575.0 | 574.4 |
| 450°C-Ti 2p3/2 | 10 | 458.6 | 458.8 |
| | 25 | 457.8 | 455.9 |
| | 40 | 456.0 | 455.8 |
| 450°C-Ni 2p3/2 | 0 | – | 858.7 |
| | 10 | 852.8 | 852.8 |
| | 25 | 852.8 | 852.8 |
| | 40 | 852.8 | 852.8 |

**Table 7 – Summary of calculated average binding energy values of core levels of different photoelectrons for oxides formed at 750 °C.**

| Photoelectron type | Thickness (nm) | $\overline{BE}_{NH}$ (eV) | $\overline{BE}_{YH}$ (eV) |
|---|---|---|---|
| 750°C-Fe 2p3/2 | 200 | 708.8 | – |
| | 360 | – | 708.9 |
| 750°C-Cr 2p3/2 | 0 | 576.5 | 576.8 |
| | 200 | 574.5 | – |
| | 360 | – | 574.4 |
| 750°C-Ti 2p3/2 | 0 | 458.3 | 458.8 |
| | 200 | 467.6 | – |
| | 360 | – | 455.2 |
| 750°C-Ni 2p3/2 | 200 | 852.8 | – |
| | 360 | – | 852.8 |

grows on, stress may be induced and therefore significantly change the growth mechanism. In addition, the doping of trace elements could somewhat alter the defect chemistry and it usually promotes the oxidation process due to the doping-induced increase of carrier concentration, which however will be neglected in the following discussion because the XPS depth profile can barely identify the existence of these doping elements such as Mo. After all, the simple analysis of oxidation for each metal element enables us to obtain a not quite rigorous, yet qualitative understanding of the formation of oxides at 450 °C and 750 °C.

For oxides obtained at 450 °C, the schematic illustration of the oxide growth process is shown in Fig. 9. Because of the high formation energy of all the related oxides (Table 4), initially the oxidation occurs simultaneously for iron, chromium and nickel, i.e. the metals donate electrons to the absorbed oxygen and form a chemical bond. In the next step, nickel and iron oxides continue to grow fast via reacting with the chemically absorbed oxygen and cation ions at the oxide/air interface, while the chromium oxide grows much more slowly due to the much smaller diffusion rate of chromium cations. For the diffusion of iron and nickel ions, though it is hard to determine which migrates fast in the oxides, based on the observed results it can be inferred that $Ni^{2+}$ migrates faster than $Fe^{3+}$ and $Fe^{2+}$, and forms an outermost layer of NiO [47].

Therefore, in the intermediate layer, there exists magnetite and hematite. The innermost layer is initially composed of scattering chromia due to the low partial pressure of oxygen inside. Taking into account the order of the formation energy for the different oxides, chromia is energetically much more stable than iron oxides, and the least stable oxide is the nickel oxides. At 450 °C, the oxidation is mainly diffusion controlled due to the formation of compact oxide layers of NiO (PBR = 1.70), hematite (PBR = 1.02 on magnetite) and magnetite (PBR = 1.2 on wustite) [32]. It should be mentioned that once these single oxides form, at the interface of those inner oxide layers it tends to react and form a more stable spinel-like phase of $FeCr_2O_4$, magnetite and $NiFe_2O_4$. According to the Raman spectra, all the nickel oxides forms the spinel-like phase. Additionally, the less stable oxides tend to be reduced by Cr and $Fe^{2+}$, which is another path for the formation of chromia and can well explained the absence of nickel oxides within the oxides. It should be mentioned that the formation of more protective spinel-like phases or corundum-like phases will further reduce the outward diffusion rate of cation and thus reduce the oxidation rate.

As for 450-YH, based on the free energy calculations (Tables 4 and 5), the iron oxides and $NiFe_2O_4$ ware preferentially reduced, and it generated the resultant metal nanoparticles, which is indirectly shown by the surface XPS results (see Fig. 8). Due to the hydrogen-induced oxygen vacancies and the small concentration of protons could enhance the transport of oxygen in oxides in the form of hydroxide ion diffusion [48]. Therefore, further oxidation occurs for the more stable phase of chromia, which agrees well with the Raman results (see Fig. 3).

When the temperature is raised to 750 °C, the concentration of both oxygen vacancies and cation vacancies increases exponentially. At the incubation stage, the oxidation process is similar to that depicted in Fig. 9, followed by the rapid growth of all oxide layers, and eventually formed the chromia and spinel phases. It is also inferred that the fast growth of oxides leads to the increase of internal stress, which can probably be caused by the formation of incompatible chromia (PBR = 2.02). Therefore, micro cracks emerged and further promoted the oxidation process, which then results in the coarsening of the surface (Fig. 3). Consequently, the oxidation process is thermodynamically controlled. According to the formation energies of all single oxides, the outermost layer should be the composite oxides composed related to titanium oxides and chromium oxides, which agrees well with the XPS results. As for 750-YH, hydrogen treatment further enhances the oxidation process and cause an increase of surface roughness (Fig. 3) and the obvious increase of oxide thickness (Fig. 7).

In brief, schematic illustration of the exact oxide structures for oxides formed at 450 °C and 750 °C without hydrogen treatment was presented in Fig. 10. The 450-NH are divided to mainly three layers, i.e. the outer layer of hematite layer dispersed with $NiFe_2O_4$, the intermediate layer being magnetite with the inclusion of scattering Ni metal particles, and the inner layer made up of titanium doped $FeCr_2O_4$, chromia, nickel and iron particles (Fig. 10(a)). The layer mainly

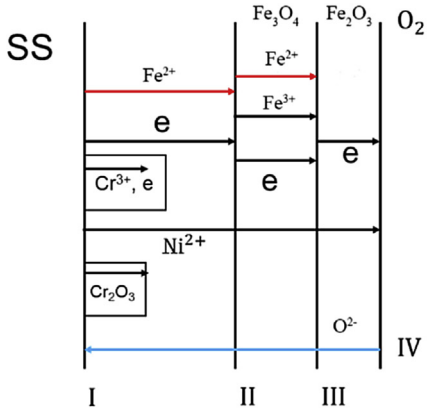


I $Fe \rightarrow Fe^{2+} + 2e'$; $Ni \rightarrow Ni^{2+} + 2e'$

$Cr \rightarrow Cr^{3+} + 3e'$; $2Cr + 3Fe^{2+} \rightarrow 2Cr^{3+} + 3Fe$

$2Cr + 3Ni^{2+} \rightarrow 2Cr^{3+} + 3Ni$

II $Fe^{2+} + 2e' + Fe_3O_4 \rightarrow 4FeO$

$Cr_2O_3 + FeO \rightarrow FeCr_2O_4$

III $2Fe^{3+} + 3O^{2-} \rightarrow Fe_2O_3$

$Fe^{n+} + ne' + 4Fe_2O_3 \rightarrow 3Fe_3O_4$ (n=2 or 3)

$2Fe^{2+} + Ni^{2+} \rightarrow 2Fe^{3+} + Ni$

IV $\frac{1}{2}O_2 + 2e' \rightarrow O^{2-}$; $Ni^{2+} + O^{2-} \rightarrow NiO$

$Ni^{2+} + 2e' + \frac{1}{2}O_2 \rightarrow NiO$; $Fe_2O_3 + NiO \rightarrow NiFe_2O_4$

**Fig. 9 – Schematic illustration of the oxide growth process for the iron-nickel based stainless steel at atmospheric pressure.**

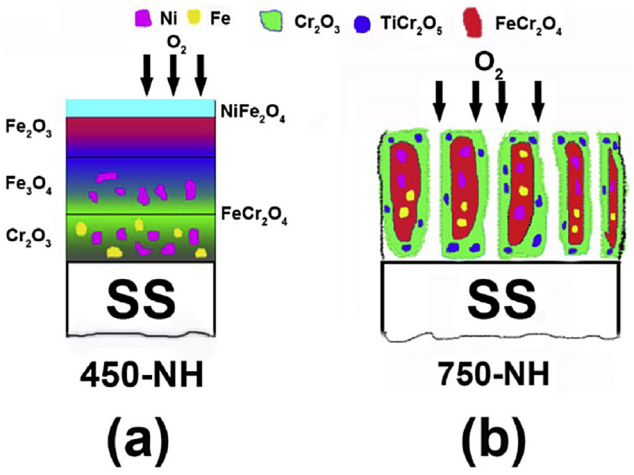


**Fig. 10 – Schematic illustration of the oxide structures formed at 450 °C and 750 °C without hydrogen permeation.**

composed of hematite, combined with $NiFe_2O_4$ and $Fe_3O_4$, display the n-type semiconductor properties while the inner $Cr_2O_3$ and $FeCr_2O_4$ shows the p-type electronic character. The decomposition of p-type feature and the drop of overall carrier concentration of n-type oxides for 450-YH are probably attributed to the reduction of iron oxides and the further oxidation of $Cr_2O_3$ and $FeCr_2O_4$, which however underwent the p-n change due to the formation of hydrogen-induced electron donors, i.e. oxygen vacancies. Therefore, it is reasonable to presume that the enhancement of the protectiveness of the inner layer originates from the further oxidation of chromium related oxides.

With regards to the oxides formed at 750 °C, it could be assumed that there mainly exist $FeCr_2O_4$ spinel and chromia with the outermost layer being chromium oxides, showing an obvious p-type semiconductor character (Fig. 10(b)). Unlike what happens to the oxides formed at 450 °C with hydrogen annealing, for 750-YH only fractional oxide shows a turn-over of the electronic character, i.e. from p-type to n-type character, probably due to the newly emergence of oxygen vacancies, while the decline of $N_A$ is assumed to originate from the decomposition of p-type phases and the possible further doping of $Fe^{2+}$ ions in $Cr_2O_3$. It is also conjectured that the obvious increase of oxide thickness results from a large amount of surface areas due to the significant increase of defects caused by the rapid oxide growth, which potentially provides myriad of sites for oxygen species adsorption and hence leads to the further oxidation. As a result, the increase of defect sites and surface roughness further decline the protectiveness of the oxide layers, which can explain the observed EIS results.

## Conclusions

Nanoscale oxide films were prepared by selective thermal oxidation, and oxides formed at 450 °C and 750 °C were selected for the subsequent study in a hydrogen environment. The oxide properties with and without hydrogen treatment are evaluated by comprehensive surface analyses. The principal findings and conclusions of this work are as follows:

(1) Oxides formed at 450 °C are mainly composed of three layers, hematite and $FeNi_2O_4$ spinel at the outermost part, intermediate layer of magnetite, and the innermost layer being $FeCr_2O_4$ and chromia. While oxides formed at 750 °C mainly constitute of chromia and $FeCr_2O_4$.
(2) Oxides formed at 450 °C exhibits p–n junction like composite semiconductor properties and demonstrates higher hydrogen resistance compared to that formed at 750 °C, which shows a predominant p-type feature and a significant surface coarsening upon hydrogen exposure.
(3) It could be inferred that the formation of p-type chromium related oxides is the main reason for its higher hydrogen resistance.

Strictly speaking, for a more exact and thorough understanding, further work such as kinetic analysis and simulation based on the first-principles and Monte Carlo calculation combined with more in-depth thermodynamic analysis will be required in the future. However, we believed that this work might provide some insights and open new door for the design of a more compatible and hydrogen resistant barrier via optimizing the composition of stainless steel or carefully manipulate the oxidation process.

## Acknowledgment

This research was funded by the NSAF program (No. U1430118), the Chinese National Fusion Project for ITER (No. 2013GB110000), the Science Challenge Project (No. JCKY2016212A504), the State Key Laboratory of Surface and Chemistry and China Academy of Engineering Physics (No. SPC 201102).

## Appendix A. Supplementary data

Supplementary data related to this article can be found at http://dx.doi.org/10.1016/j.ijhydene.2017.02.206.

## REFERENCES

[1] Odette GR, Alinger MJ, Wirth BD. Recent developments in irradiation-resistant steels. Annu Rev Mater Res 2008:471–503.
[2] Lo KH, Shek CH, Lai JKL. Recent developments in stainless steels. Mater Sci Eng R: Rep 2009;65:39–104.
[3] Shestakov V, Pisarev A, Sobolev V, Kulsartov S, Tazhibaeva I. Gas-driven deuterium permeation through F82H martensitic steel. J Nucl Mater 2002;307:1494–7.
[4] Aiello A, Ciampichetti A, Benamati G. An overview on tritium permeation barrier development for WCLL blanket concept. J Nucl Mater 2004;329:1398–402.
[5] Zajec B. Hydrogen permeation barrier - recognition of defective barrier film from transient permeation rate. Int J Hydrogen Energy 2011;36:7353–61.

[6] Nakamichi M, Kawamura H, Teratani T. Characterization of chemical densified coating as tritium permeation barrier. J Nucl Sci Technol 2001;38:1007–13.
[7] Levchuk D, Koch F, Maier H, Bolt H. Deuterium permeation through Eurofer and alpha-alumina coated Eurofer. J Nucl Mater 2004;328:103–6.
[8] Levchuk D, Levchuk S, Maier H, Bolt H, Suzuki A. Erbium oxide as a new promising tritium permeation barrier. J Nucl Mater 2007;367:1033–7.
[9] Hatano Y, Zhang K, Hashizume K. Fabrication of $ZrO_2$ coatings on ferritic steel by wet-chemical methods as a tritium permeation barrier. Phys Scr 2011:T145.
[10] Zhang GK, Wang XL, Xiong YF, Shi Y, Song JF, Luo DL. Mechanism for adsorption, dissociation and diffusion of hydrogen in hydrogen permeation barrier of alpha-$Al_2O_3$: a density functional theory study. Int J Hydrogen Energy 2013;38:1157–65.
[11] Gao JF, Suo JP, Zhang D. Self-healing behavior of pores in atmosphere plasma sprayed tritium permeation barrier coatings. Asme; 2011.
[12] Purushothaman J, Ramaseshan R, Albert SK, Rajendran R, Gowrishankar N, Ramasubbu V, et al. Influence of surface roughness and melt superheat on HDA process to form a tritium permeation barrier on RAFM steel. Fusion Eng Des 2015;101:154–64.
[13] Zhang GK, Chen CA, Luo DL, Wang XL. An advance process of aluminum rich coating as tritium permeation barrier on 321 steel workpiece. Fusion Eng Des 2012;87:1370–5.
[14] Zhang ZG, Gesmundo F, Hou PY, Niu Y. Criteria for the formation of protective $Al_2O_3$ scales on Fe-Al and Fe-Cr-Al alloys. Corros Sci 2006;48:741–65.
[15] Hatano Y, Maetani T, Sugisaki M. Characterization of surface-barrier effect upon tritium permeation through stainless-steel with auger-electron spectroscopy. Fusion Technol 1995;28:1182–7.
[16] Aiello A, Utili M, Scalia S, Coccoluto G. Experimental study of efficiency of natural oxide layers for reduction of tritium permeation through Eurofer 97. Fusion Eng Des 2009;84:385–9.
[17] Stöver D, Buchkremer HP, Hecker R, Levers HJ. Status of tritium permeation barrier development on austenitic structural alloys. J Nucl Mater 1984;123:1541–6.
[18] Cumpson PJ, Seah MP. Elastic scattering corrections in AES and XPS.2. Estimating attenuation lengths and conditions required for their valid use in overlayer/substrate experiments. Surf Interface Anal 1997;25:430–46.
[19] Sanchez-Tovar R, Leiva-Garcia R, Garcia-Anton J. Characterization of thermal oxide films formed on a duplex stainless steel by means of confocal-Raman microscopy and electrochemical techniques. Thin Solid Films 2015;576:1–10.
[20] Maslar JE, Hurst WS, Bowers WJ, Hendricks JH. In situ Raman spectroscopic investigation of stainless steel hydrothermal corrosion. Corrosion 2002;58:739–47.
[21] Woodland AB, Frost DJ, Trots DM, Klimm K, Mezouar M. In situ observation of the breakdown of magnetite ($Fe_3O_4$) to $Fe_4O_5$ and hematite at high pressures and temperatures. Am Mineralogist 2012;97:1808–11.
[22] Barker JR, Ferry DK. On the physics and modeling of small semiconductor-devices. 1. Solid-State Electron 1980;23:519–30.
[23] Fang PH, Brower WS. Dielectric constant of $Cr_2O_3$ crystals. Phys Rev 1963;129:1561.
[24] Macdonald F, Lide DR. CRC handbook of chemistry and physics: from paper to web. Abstr Pap Am Chem Soc 2003;225:U552.
[25] Feng Z, Cheng X, Dong C, Xu L, Li X. Passivity of 316L stainless steel in borate buffer solution studied by Mott–Schottky analysis, atomic absorption spectrometry and X-ray photoelectron spectroscopy. Corros Sci 2010;52:3646–53.
[26] Kim JJ, Young YM. Study on the passive film of type 316 stainless steel. Int J Electrochem Sci 2013;8:11847–59.
[27] da Cunha Belo M, Walls M, Hakiki NE, Corset J, Picquenard E, Sagon G, et al. Composition, structure and properties of the oxide films formed on the stainless steel 316L in a primary type PWR environment. Corros Sci 1998;40:447–63.
[28] Ningshen S, Mudali UK, Mittal VK, Khatak HS. Semiconducting and passive film properties of nitrogen-containing type 316LN stainless steels. Corros Sci 2007;49:481–96.
[29] Hakiki NE, Belo MD, Simoes AMP, Ferreira MGS. Semiconducting properties of passive films formed on stainless steels - influence of the alloying elements. J Electrochem Soc 1998;145:3821–9.
[30] Greeff AP, Louw CW, Swart HC. The oxidation of industrial FeCrMo steel. Corros Sci 2000;42:1725–40.
[31] Betz G, Wehner GK, Toth L. Composition-vs-depth profiles obtained with auger-electron spectroscopy of air-oxidized stainless-steel surfaces. J Appl Phys 1974;45:5312–6.
[32] Hultquist G, Leygraf C. The initiation of selective oxidation of a ferritic stainless-steel at low-temperatures and oxygen pressures. Corros Sci 1982;22:331–46.
[33] Biesinger MC, Payne BP, Grosvenor AP, Lau LWM, Gerson AR, Smart RS. Resolving surface chemical states in XPS analysis of first row transition metals, oxides and hydroxides: Cr, Mn, Fe, Co and Ni. Appl Surf Sci 2011;257:2717–30.
[34] Biesinger MC, Lau LWM, Gerson AR, Smart RSC. Resolving surface chemical states in XPS analysis of first row transition metals, oxides and hydroxides: Sc, Ti, V, Cu and Zn. Appl Surf Sci 2010;257:887–98.
[35] Kishi K. Adsorption of ethylenediamine on clean and oxygen covered Fe/Ni(100) surfaces studied by XPS. J Electron Spectrosc Relat Phenom 1988;46:237–47.
[36] Kishi K, Fujiwara K. Ultrathin nickel oxide on the $V_2O_3$ Cu(100) surface studied by XPS. J Electron Spectrosc Relat Phenom 1995;71:51–9.
[37] Zeng C, Ling YH, Bai YK, Zhang RQ, Dai X, Chen YX. Hydrogen permeation characteristic of nanoscale passive films formed on different zirconium alloys. Int J Hydrogen Energy 2016;41:7676–90.
[38] Chen WD, Wang LJ, Lu SG. Influence of oxide layer on hydrogen desorption from zirconium hydride. J Alloys Compd 2009;469:142–5.
[39] Shih C-C, Shih C-M, Su Y-Y, Su LHJ, Chang M-S, Lin S-J. Effect of surface oxide properties on corrosion resistance of 316L stainless steel for biomedical applications. Corros Sci 2004;46:427–41.
[40] Chen WK, Peterson NL. Effect of the deviation from stoichiometry on cation self-diffusion and isotope effect in wüstite, $Fe_{1-x}O$. J Phys Chem Solids 1975;36:1097–103.
[41] Peterson NL, Chen WK, Wolf D. Correlation and isotope effects for cation diffusion in magnetite. J Phys Chem Solids 1980;41:709–19.
[42] Hoshino K, Peterson NL. Cation self-diffusion and impurity diffusion in $Fe_2O_3$. J Phys Chem Solids 1985;46:1247–54.
[43] Kingery WD, Hill DC, Nelson RP. Oxygen mobility in polycrystalline $NiCr_2O_4$ and $\alpha$-$Fe_2O_3$. J Am Ceram Soc 1960;43:473–5.
[44] Atkinson A, Taylor RI. Diffusion of 55Fe in $Fe_2O_3$ single crystals. J Phys Chem Solids 1985;46:469–75.
[45] O'Keeffe M, Moore WJ. Diffusion of oxygen in single crystals of nickel oxide. J Phys Chem 1961;65:1438–9.
[46] Hoshino K, Peterson NL. Cation self-diffusion in $Cr_2O_3$. J Am Ceram Soc 1983;66:c202–3.
[47] Lobnig RE, Schmidt HP, Hennesen K, Grabke HJ. Diffusion of cations in chromia layers grown on iron-base alloys. Oxid Met 1992;37:81–93.
[48] Norby T. Protonic defects in oxides and their possible role in high temperature oxidation. J de Phys IV Colloq 1993;03. C9-99–C9-106.